Engineering Reports

WILEY

Engineering Reports Open Access

RESEARCH ARTICLE OPEN ACCESS

Microfluidic Droplet Generation Enabled by a Pressure Barrier Mechanism

Mostafa Shojaeian[1,2,3] | Ali Koşar[2,3,4]

[1]Fachgebiet Nano-und Mikrofluidik, Fachbereich Maschinenbau, Darmstadt, Germany | [2]Faculty of Engineering and Natural Sciences (FENS), Sabanci University, Istanbul, Turkey | [3]Sabanci University Nanotechnology and Application Center (SUNUM), Sabanci University, Istanbul, Turkey | [4]Center of Excellence for Functional Surfaces and Interfaces for Nano-Diagnostics (EFSUN), Sabanci University, Istanbul, Turkey

Correspondence: Ali Koşar (kosara@sabanciuniv.edu)

Received: 24 June 2025 | **Revised:** 18 December 2025 | **Accepted:** 4 January 2026

Keywords: droplet aggregation | droplet generation | microfluidics | pressure barrier

ABSTRACT

Microfluidic droplet generation enables the rapid and efficient production of large quantities of droplets to be used in various fields such as medical science and biology. While polydisperse droplets are inherent in bulk emulsion production, which can be potentially used for combinatorial experimentation in addition to monodisperse droplets, microfluidic chip platforms offer superior control for post-processing applications and are better suited for integration within miniaturized systems. In this study, we present a simple yet robust method for generating droplet aggregation, which could be used for applications where the polydisperse droplets are advantageous in the context of microfluidics. This approach offers a significantly shorter timescale (in a fraction of a second) compared to existing methods in the literature. The generated droplets rely on the hydrodynamic instability of an aqueous interface within the framework of the pressure barrier principle. This approach requires adjustments to geometry and surface wettability properties, resulting in a distinct mode of droplet generation. This approach not only leads to a platform for the water-in-air microfluidics systems but also facilitates the integration of water-in-oil emulsion into microfluidic devices as a subsequent step. It was also observed that the polydisperse droplets are only generated in Glass-PDMS chips, not PDMS-PDMS chips, and the main channel height should be critically narrow (below 10 μm in our method) to allow the system to generate droplets. The generated droplets have diameters between 1 and 7 μm, with the majority concentrated in the 2–3 μm size band.

1 | Introduction

Droplet generation is vital across a range of fields, including microfluidics, materials science, biological/biomedical applications, and environmental studies. It involves the formation of small, discrete liquid volumes (droplets) within a larger medium, typically at liquid–liquid or gas–liquid interfaces. The ability to generate droplets is crucial for their diverse applications, such as drug delivery [1], chemical reactions [2], biological assays [3], making this technology highly versatile. Droplet generation techniques can be categorized into two main types: passive and active methods [4]. Each type leverages different mechanisms and external forces to create droplets, offering its own distinct advantages and challenges. In the passive method, droplet formation occurs when one immiscible fluid (the dispersed phase) is introduced into another (the continuous phase) [5], is commonly performed in passive microfluidic devices. Active droplet generation, on the other hand, applies external power (such as electrical fields [6], pressure modulation [7] etc.) to control and manipulate the process. While passive droplet generation

is favored for its simplicity, energy efficiency, and reliability, active methods provide greater flexibility and rapid operation, allowing for more sophisticated control over the droplet formation process. The choice between passive and active methods largely depends on the application. Droplets can be generated either on-demand or in series, each approach serving different needs. On-demand droplet generation provides control over the formation and release of droplets as required [8], rather than producing them continuously or at fixed intervals. A variety of techniques, leveraging mechanical, electrical, and thermo-fluidic principles (e.g., thermal actuation and pressure-driven methods), have been developed to enable on-demand droplet generation with high accuracy [4]. High-throughput screening requires rapid and efficient production of large numbers of droplets, often at the micro- or nanoscale, that can serve as independent microreactors or miniaturized test environments [9] for many applications such as diagnostics, chemical synthesis, and biotechnology [10]. High-throughput droplet generation necessitates the combination of microfluidic technologies with materials engineering, fluid dynamics, and actuation mechanisms. Passive microfluidic systems are frequently used at the heart of high-throughput methods, where the design of microfluidic channels, such as incorporating T-junctions, flow-focusing geometries, and co-flowing fluids, plays a key role in enabling rapid and uniform droplet formation [11]. The scalability of microfluidic platforms further enhances the throughput. By integrating multiple droplet-generation units on a single microfluidic chip, large quantities of droplets can be simultaneously produced, thereby significantly improving the efficiency and enabling large-scale experiments or production processes [12]. Emulsions can be formed on bulk platforms using various approaches such as spray [13], extrusion [14], homogenization [15], and others, alongside microfluidic methods, which could be used in biomedical applications [13]. However, bulk emulsions often produce polydisperse droplets, which may require size filtering for certain analyses such as fluorescence-activated cell sorting [16].

While monodisperse droplets are ideal for many applications, polydisperse droplets are a natural outcome of various processes, both in natural and engineered systems such as atomization and spray systems [13]. Unlike monodisperse droplets, which are uniform in size, polydisperse droplets span a range of sizes, typically due to factors such as fluid flow fluctuations, variations in surface tension, or environmental conditions. These droplets are often generated in systems where precise control over the droplet size is either impractical or unnecessary, e.g., spraying. In certain applications, such as biological studies, a range of droplet sizes is not only acceptable but also advantageous [17]. The variability in the size inherent in polydisperse droplets makes them ideal for creating complex systems related to emulsions or multiphase reactions, where this heterogeneity can offer functional benefits [18]. Besides the inherent nature of polydisperse droplets in bulk emulsion production for combinatorial experimentation [13], droplet-microfluidic chip platforms (microfluidic emulsion) could be utilized for this purpose. Essentially, the concept of combinatorial droplets allows a droplet to contain multiple elements (e.g., chemical compositions, specific concentrations of materials) through the sequentially repeated merging, storage, and mixing of droplets, particularly in microfluidic devices [19]. Even with fully automated and programmed procedures, this entire process can be still time-consuming and slow to create a droplet library/array. The generation of (polydisperse) droplets, whether inside or outside microfluidic chips, serves as a powerful tool for use in different domains, such as immunoassay [20], biosensor [21], synthetic reactions (reagents) [22], single-cell combinatorics [23, 24], and combinatorial biology [25, 26], and biochemistry [27]. In most microfluidic droplet schemes, passive systems have been used to manage discrete droplets dispersed in a continuous phase. The microchannel design, coupled with the adjustment of flow rates for the dispersed and continuous phases, enables the generation, breakup, separation, and coalescence of droplets, facilitating diverse material combinations [28, 29]. Additionally, these systems can be enhanced with active strategies, such as valve-based devices, to further fine-tune and optimize the droplet generation [30].

While many state-of-the-art microfluidic systems have enabled droplet merging, collision, and controlled monodispersity using active elements such as electrowetting, valves, or thermal actuation, these methods often require complex fabrication, precise flow control, or synchronization [4]. In contrast, our approach offers a simple, passive, and fast alternative by leveraging the hydrodynamic instability at a hybrid-wettability interface, enabling a large quantity of polydisperse droplet generation without external actuation or pump adjustments. Unlike classical designs such as T-junctions or step emulsifiers that prioritize monodispersity, our method introduces a distinct, previously unreported droplet generation mode that inherently supports size variability, an advantage for applications requiring a range of droplet volumes or contents in microfluidics. Thus, we present a simple yet effective method for generating high-throughput polydisperse droplets within microfluidic chips on a millisecond timescale. The method enables not only the water-in-air microfluidics system but also water-in-oil emulsions within microfluidic devices. The main advantage lies in its potential for rapidly exploring multiple parameter combinations in a single experimental run. The objectives of this study are to develop and characterize this novel droplet generation strategy, investigate the effects of geometric and wettability parameters on droplet formation, and demonstrate the method's applicability for varying fluidic conditions in microfluidic platforms.

2 | Results and Discussion

The experiments were conducted using the microfluidic device shown in Figure 1a, with further details about the experimental setup provided in the Section 4.

2.1 | PDMS-PDMS Channel

Initial tests were conducted using channels made of entirely hydrophobic polydimethylsiloxane (PDMS), with two main shallow channel depths of 5 and 10 μm, in similar lines with our previous work [6]. It was observed that a water-air interface quickly formed for both channel depths at the junctions between the main and side channels at the expense of generating steady flow rates at Section 2, while skipping the pressure barrier at "Section 1" (i.e., no pressure barrier observed there). At the junctions, the pressure barrier successfully establishes due to the flow

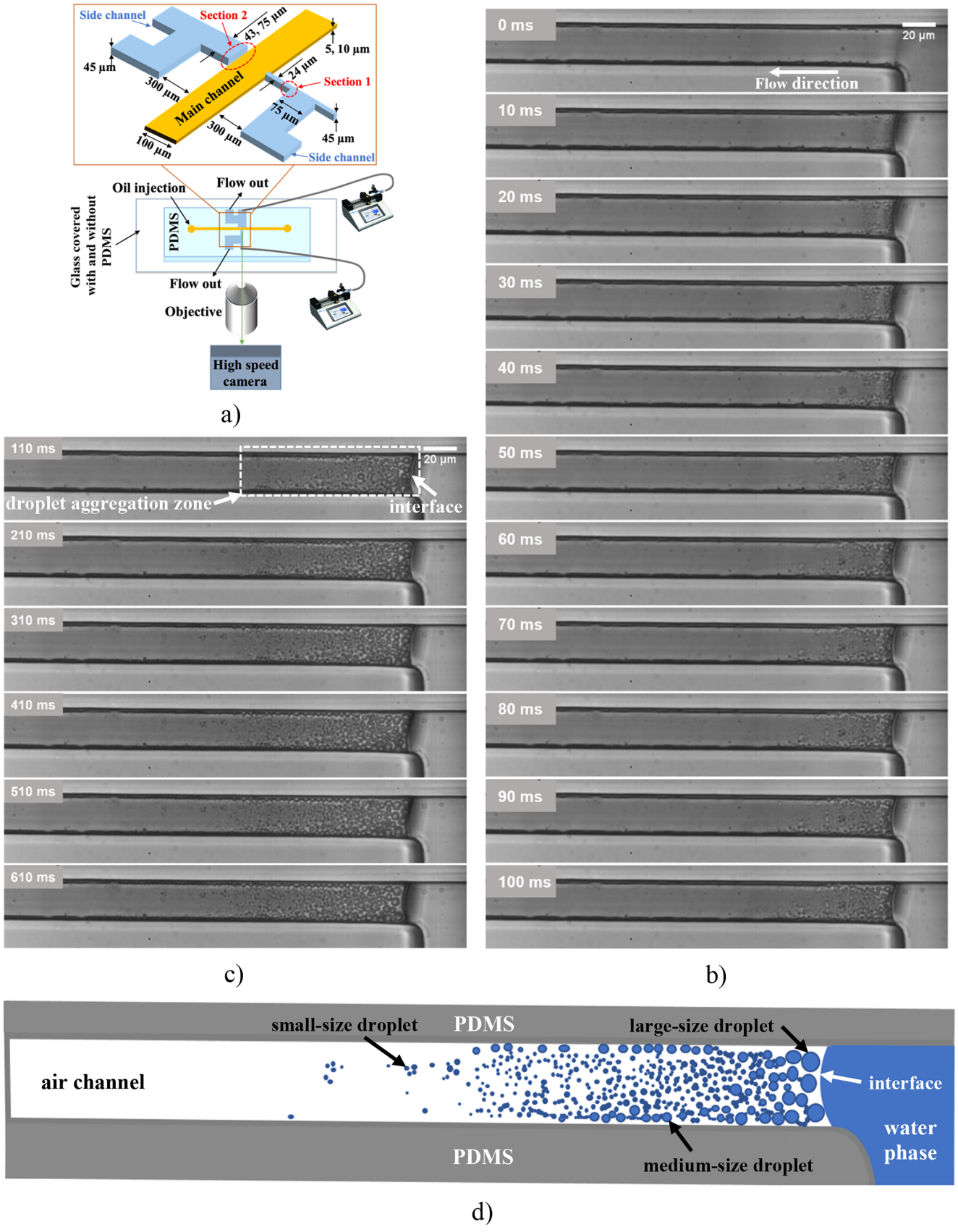

FIGURE 1 | (a) Schematic of the experimental setup. (b,c) Time-lapse images of droplet production from the water-air interface at Section 1 at the flow rate of 1000 µL/h, corresponding to the first and second stages of the process, respectively. (d) Schematic of droplet aggregation inside the microchannel, corresponding to the last time-lapse image shown in Figure 3c.

contraction and geometry dimension effect (Figure 1a). In the case of the PDMS-PDMS channel configuration, no droplet generation was observed.

2.2 | Glass-PDMS Channel

Next, we proceeded with the experiments using the hybrid wettability configuration, i.e., the PDMS-glass channel. For the main channel depth of 10 μm, the observations at Section 2 are similar to those in the previous case. No significant changes can be observed at the water-air interface. In contrast, for the channel depth of 5 μm (at Section 1 and Section 2), water-air interfaces become similarly apparent but exhibit distinctive behaviors: ejecting droplets from the interface.

If not stated otherwise, the syringe pump delivers the fluid flow to the channel from the inlet at a flow rate of 1000 μL/h. The behavior of the water-air interface at Section 1 is illustrated in Figure 1b,c, where the interface reaches the channel contraction, while the depth of the channel remains unchanged. For this case, we ran the fluid flow for a few seconds to avoid the interface occupying the whole narrow channel. For this configuration, the interface attempts to move into the narrower channel, but the pressure buildup creates a weak barrier that prevents water flow. The pressure barrier at this location (i.e., flow contraction at Section 1) is relatively weaker compared to the strong pressure barriers formed at both cross-junctions. The experimental results demonstrate that the water-air interface becomes immediately unstable, and the favorable wettability of the glass wall at the bottom of the channel, compared to the counterpart PDMS walls, contributes to the surface tension force, accelerating the destabilization of the interface. As a result, droplets shed forward from the decay of the destabilized interface (Figure 1b,c), highlighting the creation of multiple short jets from where the droplets emerge. The time-lapse images in Figure 1b,c show the droplet ejection process extending downstream in two stages. In the first stage, the droplets are smaller, and the distance along which they are ejected downstream is shorter. In the second stage, as the interface attempts to move forward, the droplet coalescence becomes more highlighted upon generation. As a result, larger droplets form along with a greater distance traveled by the droplets. The droplets near the interface are larger, while their size decreases gradually as the distance from the interface increases, appearing as a gradient droplet pattern. For further clarification, Figure 1d illustrates a schematic of the droplet aggregation inside the microchannel, corresponding to the last time-lapse image shown in Figure 1c. It is also observed that, in addition to the proximity of the interface, the droplets near the channel walls are relatively larger compared to those in the core zone of the channel. In general, when the syringe pump is switched off, the droplet aggregation remains roughly the same after some neighboring droplets get coalesced due to the highly shared interface. While some post-formation of neighboring droplets still occurs after stopping the pump, it is comparatively negligible. In this way, the polydisperse droplets can be produced in the microfluidic droplet-in-air scheme, with droplet sizes ranging from several tens of nanometers to a few micrometers in diameter. The observed polydispersity arises from the continued ejection and production of droplets during operation, along with an increased likelihood of coalescence near the water interface. In this region, resting droplets are more susceptible to interactions with incoming droplets, leading to a higher chance of merging. The mechanism of droplet formation discussed above is a bit similar to the droplet formation process at the nozzle in spraying [31]. In the spray process, droplet formation occurs in such a way that a liquid is broken up into fine droplets by factors such as the shear force, turbulence, or pressure. Typically, a liquid is forced through a nozzle under high pressure, creating a thin stream or sheet of liquid. As this stream exits the nozzle, it experiences aerodynamic forces, surface tension, and interaction with the surrounding air, which make it break apart into droplets. However, there is a difference in the droplet formation process in our method. While the water flow (i.e., interface) reaches the channel constriction (regarded as a planar nozzle) under pressure, it cannot enter the nozzle. Consequently, the forces at the nozzle exit that cause the droplet breakup could have marginal effects in our method.

In the next phase of the experiments, we supplied water to "Section 2" from the inlet using a syringe pump for 1 min. The pump was then turned off without removing the tube in order to maintain the interface at the junction. The droplet aggregation produced in the microfluidic water-in-air scheme is shown in Figure 2a for a side channel width of 43 μm. Figure 2a–f present a statistical analysis of droplets generated using our method, with a focus on postprocessing. As can be observed, the droplets can be generated in front of the junction, exhibiting a polydisperse droplet size distribution. While the droplet size can be measured manually using the ImageJ software, this process might be tedious and time-consuming. Since the interiors of the droplets are brighter than their interfaces, which resemble the background color, the CellPose tool is more effective and robust for droplet characterization and detection than ImageJ. Cellpose is an anatomical segmentation algorithm written in Python 3 by Carsen Stringer and Marius Pachitariu [32] as an open-source package that can be mainly used for cellular segmentation [33]. Therefore, we used the CellPose tool for droplet characterization, and its outputs were sent to ImageJ for size measurement. A schematic of data processing is further given in Figure S1. Figure 2b illustrates the image of the predicted droplet outlines that the Cellpose tool generated, highlighting its potential for detecting nearly all droplets. Additionally, it is important to note that the predicted outlines do not precisely align with the droplet interfaces; instead, they encircle each droplet, resulting in slightly oversized droplet representations. The overestimation of the predicted outlines for the measurement of the droplet size was found to be approximately less than 10%. The Cellpose tool, a deep learning-based segmentation method, can provide color masks and cell pose features, which in turn enable the identification of the droplet pattern as a cell-like structure (Figure 2c,d) while suppressing the droplet size overestimation. We imported the Cellpose predictions into the ImageJ software to measure the droplet size and distribution. The corresponding results, shown in Figure 2e,f, display the droplet outlines, frequency, and size distribution. The droplet size distribution, presented as a number-based frequency (i.e., the number of droplets within each size range), indicates that droplets are generated across a wide range of sizes, including small droplets. Due to the inherently polydisperse nature of the droplets generated by this method, the size distributions are presented as binned ranges rather than using mean values with standard deviations. The polydispersity

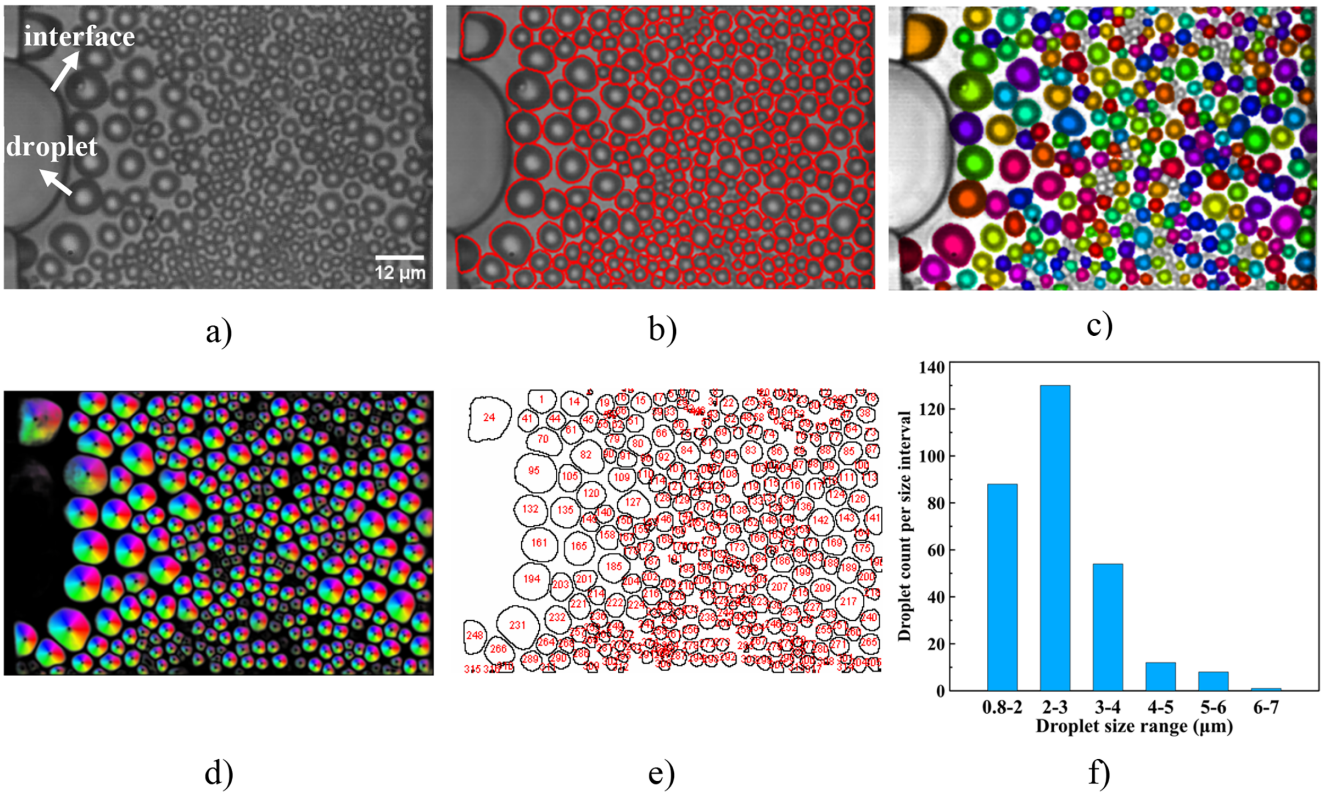

FIGURE 2 | (a) Droplet aggregation at the side channel, with a width of 43 µm, at the cross-junction (Section 2) at the flow rate of 1000 µL/h in the water-in-air system. (b) Droplet outlines predicted by the CellPose tool. (c) Color masks applied to droplets by the CellPose tool. (d) CellPose tool feature implementation for droplet identification. (e) Droplet detection and size calculation performed using the ImageJ software from the post-processed output of CellPose. (f) Droplet size distribution for the water-in-air system.

in the droplet size can be determined by the standard deviation relative to the average droplet size, which is approximately 41% in this case, suggesting a moderate droplet size distribution.

The tests also focus on the generation of a pool of droplets from the water-air interface at the junction of a larger side channel (i.e., 75 µm) and on the transition from the droplet microfluidic water-in-air scheme to the traditional water-in-oil scheme. Similar to the previous case, the water-air interface quickly reaches the junction, beyond which the syringe pump continues to operate for 1 min. Upon arrival, the interface encounters a significant pressure barrier while increasing the interface curvature. Although the interface cannot protrude into the shallow main channel, it starts to shed tiny droplets in all directions, rapidly filling the entire domain with nano-micro-scale droplet sizes. These droplets are likely generated by the formation of multiple jets, whose hydrodynamic instability produces tip-streaming droplets at the tip. Over time, the resting droplets and newly generated ones start to accumulate, making their size increase due to coalescence. This process allows droplets near the interface to grow to a larger size, as they have a higher chance of colliding with emitted droplets. As a result, droplet aggregation appears in such a way that the droplets are larger near the interface and in the middle zone, while becoming smaller toward the channel outlet. The droplet emission is so intense that it reaches the small front side channel. Figure 3a shows the droplet aggregation 30 s after the pump operation (while the pump operated for 1 min). As can be observed, very small droplets fill the main channel predominantly in front of the interface. With this approach, the droplets could be emitted at distances greater than three times the width of the side channel from where droplets emerge. In Figure 3b, the water-air interface is at rest, showing the droplet aggregation 3 min after the pump stops. The droplets here are noticeably larger compared to Figure 3a. After 10 min, the droplets grow further due to the coalescence of neighboring droplets (Figure 3c). However, it is likely that the droplet pattern stabilizes after reaching a saturation point, beyond which no further coalescence occurs. At first glance, arbitrary coalescence might be seen as an undesirable event; however, it is beneficial, as the proposed method presented here relies on droplet coalescence as well, particularly because it can potentially enable the polydisperse droplet generation.

2.3 | Water-In-Oil Droplet Generation

The studies in the literature primarily focus on producing water-in-oil droplets in microfluidic devices, utilizing the introduction of one immiscible fluid (the dispersed phase) into another (the continuous phase) as a passive mode [34]. Commonly employed configurations such as T-junctions, flow-focusing, and co-flow channels enable precise control over the droplet size and frequency by manipulating the flow rates of both phases. Here, we present a strategy for producing water-in-oil emulsion by simply dispensing silicone oil from one of the opening ports of the main channel, after the droplets are generated in air. Because the oil

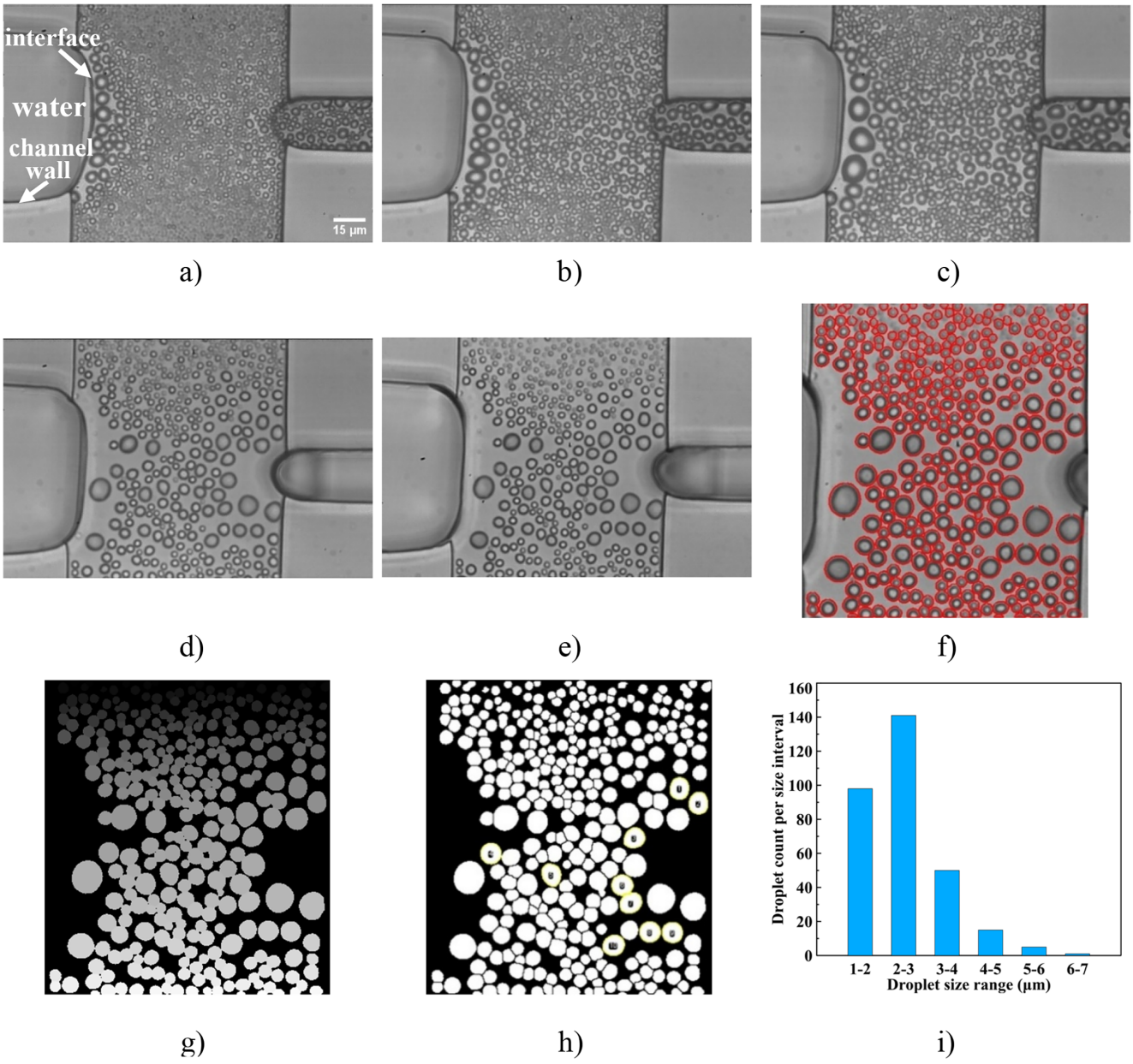

FIGURE 3 | (a) Droplet aggregation at the side channel (width = 75 μm) at the cross-junction (Section 2) at the flow rate of 1000 μL/h in the water-in-air system, 30 s after droplet generation while the pump was operating. (b) Droplet aggregation 3 min after the pump was stopped in the water-in-air system. (c) Droplet aggregation 10 min after the pump was stopped in the water-in-air system. (d) Droplet aggregation following oil dispensing (after part c) for the water-in-oil system. (e) Droplet aggregation 10 min after oil dispensing for the water-in-oil system. (f) Droplet outlines predicted by the CellPose tool corresponding to part (e). (g) Masks applied to droplets by the CellPose tool for part (e). (h) Droplet detection and size calculation performed using the ImageJ software on the post-processed output from the CellPose tool for part (e). (i) Droplet size distribution for the water-in-oil system corresponding to part (e).

readily wets the channel, it quickly fills the entire channel, containing water droplets of various sizes in air. This approach allows us to generate droplets in a range of sizes in oil. The result in Figure 3d corresponds to water-in-oil droplets immediately after dispensing the oil. The droplet size and arrangement observed in the water-in-air scheme appear to have some changes due to the influence of oil drift over the droplet aggregation. The oil drift affects the pinned droplets on the glass in various ways. Some are displaced downstream or move around, while others coalesce. The smallest droplets might have been assimilated into the oil phase. Despite these changes, a significant number of droplets remain. The droplet coalescence can be prevented by adding an appropriate oil-soluble surfactant to the oil phase before dispensing [35], or a water-soluble surfactant to the water phase is feasible if a water-air system is concerned [36]. Although the addition of oil alters the droplet aggregation in air, the resulting water droplets in oil are still important, especially when monodisperse droplets are of secondary importance [13], or when the oil phase itself is intended to activate the entities inside the droplets, as previously proven [8].

Figure 3e shows the droplet distribution in oil after a 10-min waiting time. The pattern appears to be largely unchanged compared to the moment of oil injection. This could be due to the lower density of the droplet aggregation in oil compared to water-in-air systems or a reduced tendency for droplet coalescence in oil compared to air. A further image analysis on the results was performed, and the results are shown in Figure 3e. The CellPose tool was used to obtain the predicted outline around droplets and a mask map overlaying the droplets, which are presented in Figure 3f,g, respectively. The mask output was then imported into the ImageJ software for further characterization, despite some overlaps between neighboring droplets. The original color map image (i.e., Figure 3g) was first converted to 8-bit grayscale, then segmented using a selected threshold value. To distinguish overlapping droplets, a "watershed" binary filter was applied during the processing to separate them, as seen in Figure 3h. This image was used to calculate the droplet size and to obtain the corresponding distribution, as shown in Figure 3i. The figure reveals that the droplets can be produced at different sizes, with the majority of droplets falling below 3 μm and the polydispersity of the droplets at ~33%. Unlike the microfluidic combinatorial droplet systems in the literature, which typically contain multiple elements (e.g., species concentration) formed through sequential operations such as splitting, merging, and mixing of droplets, e.g., [28], the droplet generation approach presented in this study can arbitrarily create a certain set of droplet sizes. As shown in the droplet size distributions in Figure 3i and Figure 2f, it is evident that, although the droplet generation approach here produces droplets arbitrarily, the size distribution ranges are similar, indicating rough independency from the channel width. This also suggests that the observed phenomenon or statistical results are reproducible in this arbitrary way. In addition, if droplet generators containing bulk fluids of different compositions are designed to be positioned facing each other or at an angle and generate droplets simultaneously into a shared region, the droplets encounter and mix upon formation, resulting in varied compositions suitable for combinatorial investigations. It is also worth noting that the presented method is much faster, as it eliminates the need for sequential operations and does not require programming or automation, compared to methods in the literature, e.g., [28] The size filtering was also performed using the ImageJ software. This technique is particularly useful for monitoring a specific droplet set, especially in fluorescent imaging. For example, we marked a specific droplet size range in Figure 3h, with yellow outlines and numbers.

2.4 | Flow Rate Effect

Finally, we examined the same geometry and conditions as discussed in Figure 3, but with a flow rate of 500 μL/h. The results are similar to those observed at a flow rate of 1000 μL/h, with a notable difference: the droplet aggregation domain at a flow rate of 500 μL/h is relatively smaller compared to that at 1000 μL/h, aside from the change in the droplet size frequency (to be discussed below). Video #S2 illustrates the corresponding droplet generation at a lower magnification, revealing the extent of the droplet aggregation region. The video also demonstrates the possibility of large droplets near the water-air interface to merge into the interface in the meantime. To better illustrate the initial stage of droplet formation, Figure S2 (in the Supporting Information) shows time-lapse images of the droplet aggregation evolution originating from the interface. Excluding the background noise, it is clearly evident that the droplets first appear as tiny entities, likely within the nanoscale range, with a high density near the interface. Over time, the droplets gradually grow in size owing to the coalescence of droplets. Figure S3a (in the Supporting Information) shows the droplet aggregation captured 10 min after stopping the pump, which ran for 1 min during the water-in-air droplet production process. The image in Figure S3b (in the Supporting Information) represents the same scene, i.e., Figure S3a, after the silicone oil dispensing, with the predicted droplet outlines shown in Figure S3c (in the Supporting Information). The discrepancy in the prediction of all droplets can be attributed to the blurriness of very small droplets that fell out of focus of the camera. As mentioned before, the droplet outlines would overestimate the size of droplets, as they do not exactly collapse on the droplet interfaces. Despite these limitations, the outlines can be presented to provide insight into how the introduction of oil affects the droplet population in the water-air system. In this context, the predicted droplet outlines in oil (shown in Figure S3c) were overlaid onto the image in Figure S3a. The resulting overlapped image, shown in Figure S3d, highlights that the larger droplets remain intact in both size and position, as long as they do not merge with the interface, as observed in video #S2. The droplet size distribution at the flow rate of 500 μL/h, measured 10 min after the stopping of pump operation, is compared to that at 1000 μL/h in Figure S4. The analysis was performed on the region located directly opposite the side channel section. To quantitatively characterize the droplet size distribution, we calculated the mean droplet diameter and the coefficient of variation (CV) for each flow rate condition. The CV is a normalized measure of the size variability, defined as the ratio of the standard deviation to the mean diameter (expressed as a percentage). A higher CV indicates a greater polydispersity, meaning the droplet sizes are more widely spread and less uniform, whereas a lower CV corresponds to a more monodisperse, uniform population. In our system, at 500 μL/h, the mean droplet diameter is approximately 5.5 μm with a CV of 35.3%, reflecting a moderate size variability. When increasing the flow rate to 1000 μL/h, the mean diameter decreases to 4.2 μm, with a slightly higher CV of 37.6%, indicating that although the droplets become smaller on average, their relative size variability remains similar. These metrics provide a clearer quantitative benchmark of the droplet polydispersity and its dependence on flow conditions.

3 | Conclusion

In this study, we presented a method for generating droplets inside microfluidic devices in a polydisperse manner, targeting applications where polydispersity is advantageous. Our approach exploits hydrodynamic instabilities at the water–air interface, which are triggered at channel cross-junctions and/or flow contraction regions due to the formation of a pressure barrier. The surface wettability and channel geometry are also critical factors influencing droplet formation in this system.

During droplet generation, the water-air interface creates multiple jets from which droplets are ejected, occupying the main

channel over time. These ejected droplets can accumulate on previously formed droplets, leading to the creation of larger droplets. This process enables the production of the polydisperse generated droplets inside microfluidic chips without the need for additional techniques, such as splitting and merging, or using external fields commonly employed in the literature. It was observed that polydisperse droplets with a polydispersity of around 40% or less could be generated very rapidly (in tens of milliseconds) inside microfluidic chips. The droplet aggregation follows a pattern where droplets near and across the interface tend to be larger. After producing water-in-air droplets, we further dispensed oil from the opening port to switch from a water-in-air microfluidic emulsion to a water-in-oil emulsion.

As a promising strategy, our method can be implemented in a parallel scheme, where multiple side channel units can be positioned at optimal intervals to generate a larger library of droplets in a range of sizes for both water-in-air and water-in-oil systems. Furthermore, if droplet generators carrying bulk fluids of distinct compositions are designed to be arranged to face each other or positioned at an angle, they could simultaneously produce droplets into a common region where the droplets meet and mix upon formation, yielding diverse compositions suitable for combinatorial studies.

4 | Experimental Section

4.1 | Microfluidic Chip

Experiments were conducted using the microfluidic device shown schematically in Figure 1a. The core feature of the microfluidic chip lies in its cross-junction design. A shallow main channel is positioned between two deeper side sections, creating a strong pressure barrier that prevents liquid at the side sections from flowing into the main channel. Initially, the main channel contains air, which can later be replaced with oil, while the side channels are filled with water. Each side section has a distinct configuration. One of the side sections features channels of varying widths before its cross junction, illustrated as "Section 1," while "Section 2" houses the cross-junction of the side channel of the larger width. The microfluidic chip was fabricated using a soft lithography technique [6]. An SU-8 photoresist was applied to a silicon wafer and patterned using UV lithography. The schematic of the chip fabrication is shown in Figure S5 in the Supporting Information. This patterned structure served as a mold for the chip. A mixture of polydimethylsiloxane (PDMS) and cross-linker (purchased from Dow Corning, Sylgard 184 Silicone Elastomer) was degassed in a desiccator, then cast onto the mold to form the microfluidic structures. A PDMS-to-cross-linker ratio of 10:1 was used, followed by curing at 75°C for 40 min. To create the PDMS cover, a PDMS-to-cross-linker mixture with a 20:1 ratio was spin-coated onto a glass slide at 2000 rpm for 30 s and then cured at 75°C for about 15 min. After punching the inlet and outlet holes, the chip substrate was carefully placed onto a glass slide coated with the thin PDMS layer. The assembly was then cured overnight, resulting in PDMS-PDMS bonding. This protocol was used for the channels with all surfaces made of hydrophobic PDMS. To create the PDMS-glass channels, where the substrate was replaced with glass, the PDMS bulk containing the channel configuration was bonded to the glass substrate using oxygen plasma treatment. After bonding, the assembly was cured overnight to allow the PDMS to recover its hydrophobic properties.

4.2 | Experimental Procedure

During the experiments, the main channel was filled with air, while water was introduced into the side channels through syringe pumps (KD Scientific Inc.). The pumps were continuously operated to build up the pressure and stabilize the air-water interfaces at their desired positions. A high-speed camera (Redlake Motion Pro Series Y) was mounted on an inverted microscope (Nikon Eclipse Ti) and operated at 100 fps to capture the movement and behavior of water-air interface shedding droplets. To determine the size of the produced droplets, the equivalent diameter concept was used. The visible area of each droplet was calculated with the ImageJ software (National Institute of Health, USA), and the equivalent diameter was then derived using the equation $D = (4A/\pi)^{0.5}$, where A represents the visible area of the droplet. To assess the reproducibility, the method was tested across multiple chips fabricated from different batches, and qualitatively similar results were consistently observed. For each experimental condition, three representative tests were recorded, each conducted using a different chip and/or fabrication batch to ensure the variability in the data set.

The working fluid in our experiments was water, used as the aqueous phase with a fixed salinity of 0.2 mM, achieved by adding NaCl. The oil phase was standard silicone oil with a kinematic viscosity of 100 cSt, purchased from the Sigma Aldrich company. The experiments were conducted with two different main channel depths, approximately 5 and 10 μm, and two water flow rates of 500 and 1000 μL/h. In Section 2, the channel widths at the junction are 43 and 75 μm. More details about the dimensions can be seen in Figure 1a. The flow rates were the same for both Section 1 and Section 2. It should be noted that the experiments for Section 1 and Section 2 were conducted separately, suggesting that in each experiment, only one inlet was active at a time. Two surface wettability scenarios were tested. In the first scenario, all channel surfaces were hydrophobic PDMS, as discussed above. In the second scenario, a hybrid configuration, the top and sides of the channel surfaces were fully hydrophobic (PDMS), exhibiting a water contact angle of between 105° to 110° [37], while the bottom surface was hydrophilic (glass slide) with a contact angle of 19° [38].

In the case of the water–oil system, which was produced following the water–air droplet generation, the water droplets in the oil were formed by simply dispensing the oil from the inlet of the main channel. The oil then wetted the channel walls and flowed through the channel by capillary action, covering the water droplets that had previously been generated in the air. The corresponding imaging was performed after the oil flow filled the channel and stopped.

Acknowledgments

Mostafa Shojaeian kindly acknowledges the support from the LOEWE CompuGene Project, funded by the Hessian Ministry of Science and Art.

Funding

This work was supported by the Hessisches Ministerium für Wissenschaft und Kunst (LOEWE CompuGene Project).

Conflicts of Interest

The authors declare no conflicts of interest.

Data Availability Statement

The data will be available upon request.

References

1. C. X. Zhao, "Multiphase Flow Microfluidics for the Production of Single or Multiple Emulsions for Drug Delivery," *Advanced Drug Delivery Reviews* 65, no. 11–12 (2013): 1420–1446, https://doi.org/10.1016/j.addr.2013.05.009.

2. K. S. Elvira, X. C. I. Solvas, R. C. R. Wootton, and A. J. Demello, "The Past, Present and Potential for Microfluidic Reactor Technology in Chemical Synthesis," *Nature Chemistry* 5, no. 11 (2013): 905–915, https://doi.org/10.1038/nchem.1753.

3. M. T. Guo, A. Rotem, J. A. Heyman, and D. A. Weitz, "Droplet Microfluidics for High-Throughput Biological Assays," *Lab on a Chip* 12, no. 12 (2012): 2146–2155, https://doi.org/10.1039/c2lc21147e.

4. P. Zhu and L. Wang, "Passive and Active Droplet Generation With Microfluidics: A Review," *Lab on a Chip* 17, no. 1 (2017): 34–75, https://doi.org/10.1039/C6LC01018K.

5. A. Ahmadpour, M. Shojaeian, and S. Tasoglu, "Deep Learning-Augmented T-Junction Droplet Generation," *iScience* 27, no. 4 (2024): 109326, https://doi.org/10.1016/j.isci.2024.109326.

6. M. Shojaeian and S. Hardt, "Mass Transfer via Femtoliter Droplets in Ping-Pong Mode," *Physical Review Applied* 13, no. 1 (2020): 014015, https://doi.org/10.1103/PhysRevApplied.13.014015.

7. H. Zhou and S. Yao, "A Facile On-Demand Droplet Microfluidic System for Lab-On-a-Chip Applications," *Microfluidics and Nanofluidics* 16, no. 4 (2014): 667–675, https://doi.org/10.1007/s10404-013-1268-8.

8. M. Shojaeian, F. X. Lehr, H. U. Göringer, and S. Hardt, "On-Demand Production of Femtoliter Drops in Microchannels and Their Use as Biological Reaction Compartments," *Analytical Chemistry* 91, no. 5 (2019): 3484–3491, https://doi.org/10.1021/acs.analchem.8b05063.

9. E. M. Payne, D. A. Holland-Moritz, S. Sun, and R. T. Kennedy, "High-Throughput Screening by Droplet Microfluidics: Perspective Into Key Challenges and Future Prospects," *Lab on a Chip* 20, no. 13 (2020): 2247–2262, https://doi.org/10.1039/d0lc00347f.

10. L. Zhang, R. Parvin, M. Chen, D. Hu, Q. Fan, and F. Ye, "High-Throughput Microfluidic Droplets in Biomolecular Analytical System: A Review," *Biosensors & Bioelectronics* 228 (2023): 115213, https://doi.org/10.1016/j.bios.2023.115213.

11. G. T. Vladisaljević, "Droplet Microfluidics for High-Throughput Screening and Directed Evolution of Biomolecules," *Micromachines (Basel)* 15, no. 8 (2024): 971, https://doi.org/10.3390/mi15080971.

12. S. Zhang, K. Wang, and G. Luo, "High-Throughput Generation of Uniform Droplets From Parallel Microchannel Droplet Generators and the Preparation of Polystyrene Microsphere Material," *Particuology* 77 (2023): 136–145, https://doi.org/10.1016/j.partic.2022.10.010.

13. R. Fukuda and N. J. Cira, "High-Throughput, Combinatorial Droplet Generation by Sequential Spraying," *Lab on a Chip* (2024): 1502–1511, https://doi.org/10.1039/d4lc00656a.

14. T. Pereira, T. J. Millar, and J. A. Chuck, "Viability Analysis of Alginate Encapsulated Micro-Organisms Using Fluorescent Stains," *Journal of Microencapsulation* 22, no. 7 (2005): 787–792, https://doi.org/10.1080/02652040500273829.

15. S. Schultz, G. Wagner, K. Urban, and J. Ulrich, "High-Pressure Homogenization as a Process for Emulsion Formation," *Chemical Engineering & Technology* 27, no. 4 (2004): 361–368, https://doi.org/10.1002/ceat.200406111.

16. T. Katsuragi, S. Tanaka, S. Nagahiro, and Y. Tani, "Gel Microdroplet Technique Leaving Microorganisms Alive for Sorting q by Flow Cytometry," *Journal of Methods Microbiological Journal of Microbiological Methods* 42 (2000): 81–86, https://doi.org/10.1016/S0167-7012(00)00179-2.

17. S. A. Byrnes, E. A. Phillips, T. Huynh, B. H. Weigl, and K. P. Nichols, "Polydisperse Emulsion Digital Assay to Enhance Time to Detection and Extend Dynamic Range in Bacterial Cultures Enabled by a Statistical Framework," *Analyst* 143, no. 12 (2018): 2828–2836, https://doi.org/10.1039/c8an00029h.

18. S. A. Byrnes, T. C. Chang, T. Huynh, A. Astashkina, B. H. Weigl, and K. P. Nichols, "Simple Polydisperse Droplet Emulsion Polymerase Chain Reaction With Statistical Volumetric Correction Compared With Microfluidic Droplet Digital Polymerase Chain Reaction," *Analytical Chemistry* 90, no. 15 (2018): 9374–9380, https://doi.org/10.1021/acs.analchem.8b01988.

19. S. H. Jin, H. H. Jeong, B. Lee, S. S. Lee, and C. S. Lee, "A Programmable Microfluidic Static Droplet Array for Droplet Generation, Transportation, Fusion, Storage, and Retrieval," *Lab on a Chip* 15, no. 18 (2015): 3677–3686, https://doi.org/10.1039/c5lc00651a.

20. S. A. Byrnes, T. Huynh, T. C. Chang, et al., "Wash-Free, Digital Immunoassay in Polydisperse Droplets," *Analytical Chemistry* 92, no. 5 (2020): 3535–3543, https://doi.org/10.1021/acs.analchem.9b02526.

21. Z. Wang, N. Feng, Y. Zhou, et al., "Mesophilic Argonaute-Mediated Polydisperse Droplet Biosensor for Amplification-Free, One-Pot, and Multiplexed Nucleic Acid Detection Using Deep Learning," *Analytical Chemistry* 96, no. 5 (2024): 2068–2077, https://doi.org/10.1021/acs.analchem.3c04426.

22. A. B. Theberge, E. Mayot, A. El Harrak, F. Kleinschmidt, W. T. S. Huck, and A. D. Griffiths, "Microfluidic Platform for Combinatorial Synthesis in Picolitre Droplets," *Lab on a Chip* 12, no. 7 (2012): 1320–1326, https://doi.org/10.1039/c2lc21019c.

23. C. A. Lareau, F. M. Duarte, J. G. Chew, et al., "Droplet-Based Combinatorial Indexing for Massive-Scale Single-Cell Chromatin Accessibility," *Nature Biotechnology* 37, no. 8 (2019): 916–924, https://doi.org/10.1038/s41587-019-0147-6.

24. R. Xie, Y. Liu, S. Wang, et al., "Combinatorial Perturbation Sequencing on Single Cells Using Microwell-Based Droplet Random Pairing," *Biosensors & Bioelectronics* 220 (2023): 220, https://doi.org/10.1016/j.bios.2022.114913.

25. J. Cao, D. A. Russo, T. Xie, G. A. Groß, and J. A. Z. Zedler, "A Droplet-Based Microfluidic Platform Enables High-Throughput Combinatorial Optimization of Cyanobacterial Cultivation," *Scientific Reports* 12, no. 1 (2022): 15536, https://doi.org/10.1038/s41598-022-19773-6.

26. S. Antona, T. Abele, K. Jahnke, et al., "Droplet-Based Combinatorial Assay for Cell Cytotoxicity and Cytokine Release Evaluation," *Advanced Functional Materials* 30, no. 46 (2020): 2003479, https://doi.org/10.1002/adfm.202003479.

27. M. Benz, M. R. Molla, A. Böser, A. Rosenfeld, and P. A. Levkin, "Marrying Chemistry With Biology by Combining On-Chip Solution-Based Combinatorial Synthesis and Cellular Screening," *Nature Communications* 10, no. 1 (2019): 2879, https://doi.org/10.1038/s41467-019-10685-0.

28. E. Um, M. E. Rogers, and H. A. Stone, "Combinatorial Generation of Droplets by Controlled Assembly and Coalescence," *Lab on a Chip* 13, no. 23 (2013): 4674–4680, https://doi.org/10.1039/c3lc50957e.

29. K. Hsieh, H. C. Zec, P. C. Ma, T. D. Rane, and T. H. Wang, "Enhancing Throughput of Combinatorial Droplet Devices via Droplet Bifurcation,

Parallelized Droplet Fusion, and Parallelized Detection," *Micromachines* 6, no. 10 (2015): 1490–1504, https://doi.org/10.3390/mi6101434.

30. H. Li, P. Zhang, K. Hsieh, and T. H. Wang, "Combinatorial Nanodroplet Platform for Screening Antibiotic Combinations," *Lab on a Chip* 22, no. 3 (2022): 621–631, https://doi.org/10.1039/d1lc00865j.

31. S. Sazhin, *Droplets and Sprays*, vol. 345 (Springer, 2014), https://doi.org/10.1007/978-1-4471-6386-2.

32. C. Stringer and M. Pachitariu, Cellpose-SAM: Superhuman Generalization for Cellular Segmentation, http://www.cellpose.org/.

33. C. Stringer, T. Wang, M. Michaelos, and M. Pachitariu, "Cellpose: A Generalist Algorithm for Cellular Segmentation," *Nature Methods* 18, no. 1 (2021): 100–106, https://doi.org/10.1038/s41592-020-01018-x.

34. M. Shojaeian and S. Hardt, "Fast Electric Control of the Droplet Size in a Microfluidic T-Junction Droplet Generator," *Applied Physics Letters* 112, no. 19 (2018): 194102, https://doi.org/10.1063/1.5025874.

35. M. Zembyla, B. S. Murray, and A. Sarkar, "Water-In-Oil Emulsions Stabilized by Surfactants, Biopolymers and/or Particles: A Review," *Trends in Food Science & Technology* 104 (2020): 49–59, https://doi.org/10.1016/j.tifs.2020.07.028.

36. K. L. Pan, Y. H. Tseng, J. C. Chen, K. L. Huang, C. H. Wang, and M. C. Lai, "Controlling Droplet Bouncing and Coalescence With Surfactant," *Journal of Fluid Mechanics* 799 (2016): 603–636, https://doi.org/10.1017/jfm.2016.381.

37. B. Ruben, M. Elisa, L. Leandro, et al., "Oxygen Plasma Treatments of Polydimethylsiloxane Surfaces: Effect of the Atomic Oxygen on Capillary Flow in the Microchannels," *Micro & Nano Letters* 12, no. 10 (2017): 754–757, https://doi.org/10.1049/mnl.2017.0230.

38. J. X. H. Wong and H. Z. Yu, "Preparation of Transparent Superhydrophobic Glass Slides: Demonstration of Surface Chemistry Characteristics," *Journal of Chemical Education* 90, no. 9 (2013): 1203–1206, https://doi.org/10.1021/ed300809m.

Supporting Information

Additional supporting information can be found online in the Supporting Information section. **Figure S1:** Schematic data processing used for obtaining the droplet size distribution. **Figure S2:** Time-lapse images of the initial moments of the droplet production from the water-air interface at Section 1 at the flow rate of 500 μL/h. **Figure S3:** (a) Droplet aggregation at the side channel (width = 75 μm) at the cross-junction (Section 2) at the flow rate of 500 μL/h in the water-in-air system, 10 min after the pump was stopped in the water-in-air system, (b) Droplet aggregation following oil dispensing (after part (a) representing the water-in-oil system, (c) droplet outlines predicted by the CellPose tool and processed with the ImageJ software, corresponding to part (b), (d) Overlay of droplet outlines from the water-in-oil system in part (b) onto the droplet aggregation from the water-in-air system in part (a). **Figure S4:** Comparison of droplet size distributions of the water-in-air system at flow rates of 500 μL/h and 1000 μL/h, measured 10 min after pump operation was stopped. The analysis was conducted in the region located directly opposite the side channel section. Droplet size distribution for the water-in-oil system. **Figure S5:** Schematic protocol for fabricating Glass-PDMS and PDMS-PDMS microfluidic chips. **Video S1:** Droplet generation inside main channel at Section 2 at 1000 μL per hour.avi. **Video S2:** Droplet generation inside main channel at Section 2 at 500 μL per hour.avi.